CHAPTER II

LINEAR WAVE PACKET INTERFEROMETRY

Linear wave packet interferometry (WPI), originally developed by Scherer et al.,[1,2] uses a pair of phase-locked pulses to excite a superposition of two nuclear wave packets in an excited-electronic level. Subsequent detection of the electronic population as a function of the phase-locking angle is used to isolate the interference contribution to the population, where the latter arises from the overlap between one-pulse wave packets excited by the phase-locked pulse-pair. This bilinear interference is a probe of the prepared electronic *amplitude* and, coupled with adequate knowledge about the underlying Hamiltonian, provides an experimental means to reconstruct the nuclear wave packet excited by one of the pulses.

In this chapter, we review the theoretical development of linear WPI and show which combinations of measurements isolate the interference population. We discuss how the interference probes the delay-dependent overlap between one-pulse wave packets. We also review quantum state holography (QSH),[3,4] which uses the interferogram to reconstruct a one-pulse wave packet localized at the Franck-Condon transition point. We analyze in detail the linear WPI signal for a model harmonic system using analytic forms of the wave packets and their interference. The simulated interference signal is interpreted with help of phase-space diagrams to describe the harmonic wave-packet motion.

Theory

In linear WPI each member of the pulse-pair drives an electronic transition between an initial electronic level $|g\rangle$ and an final electronic level $|f\rangle$. The molecular Hamiltonian, in the absence of the fields, is

$$H = |g\rangle H_g \langle g| + |f\rangle H_f \langle f| , \tag{2.1}$$

where H_g and H_f are the nuclear Hamiltonians of the initial (g) and final (f) electronic levels. The total time-dependent Hamiltonian is expressed as $H(t) = H + V(t)$ with the time-dependent matter-field interaction given by

$$V(t) = V_1(t) + V_2(t) . \tag{2.2}$$

The jth interaction $(j = 1,2)$ is expressed in the electric-dipole approximation as

$$V_j(t) = \quad \mathbf{E}_j(t) , \tag{2.3}$$

where the dipole-moment operator

$$= \quad {}_{fg}\left(|f\rangle\langle g| + |g\rangle\langle f|\right) \tag{2.4}$$

couples the electronic levels g and f via the dipole moment vector ${}_{fg}$. The jth electric field is represented in the time domain by

$$\mathbf{E}_j(t) = \mathbf{e}_j A_j\left(t \quad t_j\right)\cos \quad {}_j\left(t \quad t_j\right), \tag{2.5}$$

where $\mathbf{e}_j$ is the polarization vector, $A_j(t)$ is the temporal envelope centered at time t_j, and ${}_j(t)$ is the temporal phase function. A timeline of the pulse-pair is show in Fig 2.1.

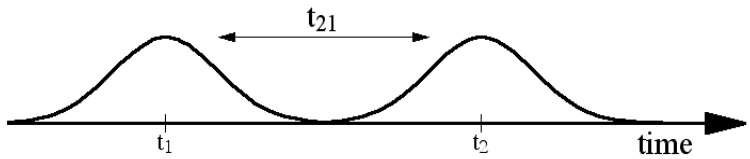

Fig. 2.1 A timeline of the pulse-pair used in a linear WPI experiment.

Phase-locking fixes the relative spectral phase between pulses at a specific locking frequency. We define the Fourier component of the jth field at frequency as

$$_{j}(\ )e^{\ i\ _{j}(\ )+i\ \ t_{j}} = e^{i\ \ t_{j}}\ \ dte^{i\ \ t}A_{j}(t)\cos\ \ _{j}(t), \tag{2.6}$$

with $_{j}(\ )$ the spectral amplitude and $_{j}(\ )\ \ t_{j}$ the spectral phase. Phase-locking the pulse-pair at frequency $_{L}$ defines the phase-locking angle

$$= \ _{2}(\ \ _{L})\ \ \ _{1}(\ \ _{L})\ \ \ _{L}t_{21}, \tag{2.7}$$

where we denote the intra-pulse delay as $t_{21} = t_{2}\ \ t_{1}$. One challenging aspect of phase-locking optical pulses is that slight variations in the intra-pulse delay lead to large variations in the spectral phase difference. Given unavoidable fluctuations in pathlength, Scherer and coworkers employed an actively stabilized phase-locking setup, based on the spectral interference between the pulses, to monitor and control the phase-locking angle.[1] The ability to do so is an important component for detection of the interference signal, which is linear in the phase-locking angle .

Well before the arrival of either pulse, the molecule is assumed to populate the initial electronic level g and the molecular amplitude is written as

$$\left|\ \ (t << t_{1,2})\right\rangle = |g\rangle e^{\ iH_{g}(t\ \ t_{1})}\left|\ \ _{g}\right\rangle, \tag{2.8}$$

where $\left| \quad {}_g \right\rangle$ is an eigenstate of H_g with eigenenergy $E_g\left(\quad {}_g \right)$ and we set $\hbar = 1$. We solve Schrödinger's equation,

$$i\frac{\left| \quad (t) \right\rangle}{t} = H(t)\left| \quad (t) \right\rangle,$$

to calculate the molecular amplitude following the pulse sequence. First, we transform to the interaction picture, defined by the unitary transformation

$$\left| \tilde{} \ (t) \right\rangle = e^{iHt}\left| \quad (t) \right\rangle, \tag{2.9}$$

and then solve the corresponding equation of motion,

$$i\frac{\left| \tilde{} \ (t) \right\rangle}{t} = \tilde{V}(t)\left| \tilde{} \ (t) \right\rangle, \tag{2.10}$$

where the latter is driven by the interaction operator

$$\tilde{V}(t) = e^{iHt}V(t)e^{\ iHt}. \tag{2.11}$$

Integrating Eq. (2.10), we obtain the formal solution

$$\left| \tilde{} \ (t) \right\rangle = \left| \tilde{} \ (t_0) \right\rangle \quad i\int_{t_0}^{t} d \ \tilde{V}(t)\left| \tilde{} \ (t) \right\rangle, \tag{2.12}$$

where the initial time t_0 is well before the arrival of either pulse. The initial condition of Eq. (2.8) then becomes

$$\left| \tilde{} \ (t_0) \right\rangle = |g\rangle e^{iH_g t_1}\left| \quad {}_g \right\rangle. \tag{2.13}$$

The molecular amplitude in Eq. (2.12) is exact and can be solved using numerical integration. However, to highlight the role of phase-locking in the preparation of the *f*-

state nuclear amplitude, we take the weak-field limit and expand the solution (2.12) out to first order in the interaction $V(t)$. The resulting perturbative expansion is[5]

$$\left|\tilde{\ }(t)\right\rangle \quad \left|\tilde{\ }(t_0)\right\rangle \quad i\int_{t_0}^{t} dt V(t)\left|\tilde{\ }(t_0)\right\rangle. \tag{2.14}$$

Projecting out the *f*-state nuclear amplitude yields

$$\left\langle f\right|\tilde{\ }(t)\left\rangle = \quad i \quad dt\left\langle f\right|\tilde{V}(t)\left|g\right\rangle e^{iH_g t_1}\left|\ _g\right\rangle. \tag{2.15}$$

In going to Eq. (2.15), we have inserted the initial condition given by Eq. (2.13) and replaced the upper/lower limit of integration by $+/\quad$. The latter substitutions reflect that the observation time t is after the action of the last pulse and the initial time t_0 is before the interaction $V(t)$ turns on.

Recalling Eqs. (2.2) and (2.11), we find from Eq. (2.15) the *f*-state nuclear amplitude following the last pulse to be

$$\left\langle f\right|\tilde{\ }(t)\left\rangle = \quad i \quad dt\left\langle f\right|\tilde{V}_1(t)\left|g\right\rangle \quad i \quad dt\left\langle f\right|\tilde{V}_2(t)\left|g\right\rangle\Big(e^{iH_g t_1}\left|\ _g\right\rangle. \tag{2.16}$$

Each integral on the RHS of Eq. (2.16) represents preparation of a nuclear wave packet in the *f*-electronic level. For the jth pulse, we rewrite the excitation operator as

$$i \quad dt\left\langle f\right|\tilde{V}_j(t)\left|g\right\rangle = i \quad d \quad e^{iH_f} \quad _{fg} \quad \mathbf{e}_j e^{\ iH_g} \ A_j\Big(\quad t_j\Big)\cos \quad _j\Big(\quad t_j\Big) \tag{2.17}$$

$$= e^{iH_f t_j} P_j^{fg} e^{\ iH_g t_j}.$$

In going to the last line of Eq. (2.17), we introduce the pulse propagator

$$P_j^{fg} = i \quad d \;\; e^{iH_f} \quad {}_{fg} \;\; \mathbf{e}_j e^{\;iH_g} \; A_j(\;\;)\cos \quad {}_j(\;\;) \tag{2.18}$$

to describe the transfer of nuclear amplitude from g to f via the jth field. It is seen immediately that the amount of amplitude transferred by the pulse propagator is proportional to the pulse spectrum at the Bohr resonance frequency; using the nuclear eigenstates of the g and f Hamiltonians, we express the pulse propagator as

$$\left\langle \;\; {}_f \middle| P_j^{fg} \middle| \;\; {}_g \right\rangle = i \left\langle \;\; {}_f \middle| \;\; {}_{fg} \;\; \mathbf{e}_j \middle| \;\; {}_g \right\rangle \;\; d \;\; A_j(\;\;)\cos \quad {}_j(\;\;) e^{i\left(E_f(\;\;{}_f) \;\; E_g(\;\;{}_g)\right)} \tag{2.19}$$

$$= i \left\langle \;\; {}_f \middle| \;\; {}_{fg} \;\; \mathbf{e}_j \middle| \;\; {}_g \right\rangle \;\; {}_j\left(E_f(\;\;{}_f) \quad E_g(\;\;{}_g)\right) e^{\;i \;\; {}_j\left(E_f(\;\;{}_f) \;\; E_g(\;\;{}_g)\right)},$$

where we have used definition of the pulse spectrum given in Eq. (2.6).

From Eq. (2.17), the f-state amplitude is rewritten as

$$\left\langle f \middle| \;\; {}^{\sim} \left(t >> t_2\right)\right\rangle = e^{iH_f t_2} \left(\left| (1)_f \right\rangle + \left| (2)_f \right\rangle e^{\;i} \;\; \right), \tag{2.20}$$

where the nuclear wave packet prepared by the first and second pulses are defined as

$$\left| (1)_f \right\rangle = e^{\;iH_f t_{21}} P_1^{fg} \left| \;\; {}_g \right\rangle \tag{2.21}$$

and

$$\left| (2)_f \right\rangle = P_2^{fg} e^{\;iH_g t_{21}} \left| \;\; {}_g \right\rangle, \tag{2.22}$$

respectively. The wave packets above are defined for the case that the phase-locking angle is set to zero; i.e. $= 0$. For an arbitrary value of the phase-locking angle, the second-pulse wave packet acquires a shift in phase and the accompanying phase factor in Eq. (2.20) explicates this dependence. We also include back-propagation of the wave

packets in Eq. (2.20) in anticipation of returning to the Schrödinger picture. The preparation processes leading to the one-pulse wave packets are illustrated in Fig. 2.2.

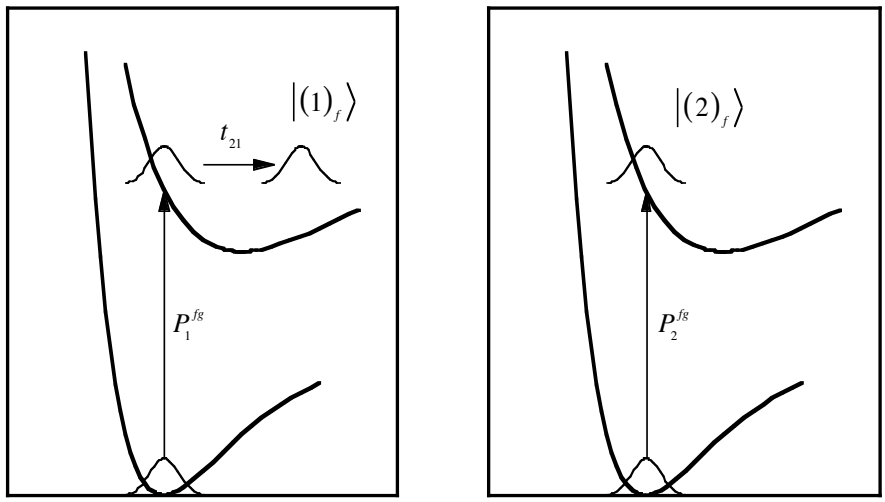

Fig. 2.2 A schematic illustration of the molecular system under consideration in a linear WPI experiment. Vertical lines denote resonant excitations between the initial (*g*) and final (*f*) potential surfaces. By varying the pulse parameters, the interference between these one-pulse wave packets can be isolated.

Transforming back to the Schrödinger picture via the inverse of Eq. (2.9), we find for $t >> t_2$ the *f*-state amplitude is given by

$$\langle f| \quad (t >> t_2)\rangle = e^{\ iH_f(t\ \ t_2)}\ |(1)_f\rangle + |(2)_f\rangle e^{\ i} \quad . \tag{2.23}$$

The population of the *f*-electronic level is the magnitude of the amplitude,

$$P_f = |\langle f| \quad (t)\rangle|^2 ,$$

which, after inserting Eq. (2.23), becomes

$$P_f(\ \ ) = \langle (1)_f|(1)_f\rangle + \langle (2)_f|(2)_f\rangle \tag{2.24}$$

$$+ \langle (1)_f|(2)_f\rangle e^{\ i} + \langle (2)_f|(1)_f\rangle e^{i} \ .$$

In Eq. (2.24), the first line represents the two one-pulse contributions to the population, while the second line comprises contributions to the population resulting from wave packet interference. The latter contribution is bilinear in the electric-field amplitudes and varies as a function of both the intra-pulse delay and the experimentally-controlled phase-locking angle. The bilinear interference constitutes the sought-after linear WPI signal.

The sign of the bilinear interference term is controlled by the phase-locking angle. Consequently, the bilinear interference may be isolated by combining measurements of the total population taken with different values of the phase-locking angle. We express Eq. (2.24) as the (Fourier) series

$$P_f(\ ) = \sum_{m=\ 1}^{1} p_m e^{im} \ , \tag{2.25}$$

where the coefficients are given as

$$p_0 = \left\langle (1)_f \middle| (1)_f \right\rangle + \left\langle (2)_f \middle| (2)_f \right\rangle \tag{2.26}$$

and

$$p_1 = \left\langle (2)_f \middle| (1)_f \right\rangle \tag{2.27}$$

with $p_{\ 1} = p_1$. The expression for the population given by Eq. (2.25) is completely specified by the three independent parameters in Eq. (2.26) and (2.27); p_0, $\mathrm{Re}\, p_1$, and $\mathrm{Im}\, p_1$. From the orthogonality of the plane wave basis, these coefficients can be recovered from measurements of the population as[6]

$$p_m = \frac{1}{2} \quad P_f(\ )e^{\ im}\, d \quad . \tag{2.28}$$

Equation (2.28) provides an analytic means by which population measurements can be used to isolate wave packet interferences; yet, Eq. (2.28) may be impractical for experimental determination of the bilinear wave packet interference p_1, as it requires continuous sampling of the *f*-state population with respect to the phase-locking angle. Furthermore, the finite form of Eq. (2.25) suggest only a few measurements should be necessary to isolate each component. Therefore, we determine the conditions under which Eq. (2.28) can be reduced to a finite sum of population measurements.

Realistically, we assume the *f*-state population is sampled at evenly-spaced values of the phase-locking angle with an interval between values. The possible phase-locking angles are then integer multiples of defined by

$$_k = k \tag{2.29}$$

for $k = 0,1,2,...K \quad 1$. We take the integer K such that $_K = 2$ and the sampling interval is defined as $= 2 \quad / K$. According to the sampling theorem,[7] accurate recovery of each Fourier coefficient requires the sampling frequency $2 \quad ^1$ to be greater than the bandwidth of Eq. (2.25). The latter is $2N = 3$ and from the sampling theorem requires $K \quad 2N + 1 = 3$. Hence, interference isolation necessitates a minimum number of $K = 3$ measurements and a sampling interval of $= 2 \quad / 3$. Then the integral in Eq. (2.28) reduces to a finite sum over these discretely-sampled data, and yields

$$p_m = \frac{1}{K} \sum_{k=0}^{K \quad 1} P_f(k \quad)e^{\ imk} \tag{2.30}$$

$$= \frac{1}{3} \sum_{k=0}^{2} P_f(2 \quad k/3) e^{\quad i2 \quad mk/3}.$$

Considering three independent quantities describe the population in Eq. (2.25), it seems intuitive that a minimum of three measurements should be required to isolate each Fourier coefficient. However, Eq. (2.30) gives not only which measurements are necessary for interference isolation, but the manner in which the signals should be combined. Specifically, for the bilinear interference p_1, Eq. (2.30) yields

$$p_1 = \frac{1}{3}\left(P_f(0) + P_f(\quad) e^{\quad i} + P_f(2 \quad) e^{i}\right), \tag{2.31}$$

while the sum of one-pulse contributions to the population is

$$p_0 = \frac{1}{3}\left(P_f(0) + P_f(\quad) + P_f(2 \quad)\right). \tag{2.32}$$

As a consequence of the sampling theorem, the use of a sampling interval smaller than the critical sampling interval does not provide additional information about the interferences and is therefore unnecessary from a theoretical standpoint. Experimentally, however, certain sampling intervals may be more practical or more easily implemented. Such was the case in the linear WPI experiments performed by Scherer *et al.*,[1,2] where population measurements were taken with a sampling interval of $= 2 \quad / 4$, i.e. $K = 4$. A feedback controlled phase-locking apparatus monitored the phase-locking angle by detecting fluctuations in the first and second derivatives of the spectral interference which are minimized for in-phase and in-quadrature values of locking angle, respectively. For this case, using the first line of Eq. (2.30), the bilinear interference isolation is given by

$$p_1 = \frac{1}{4}\left(P_f(0) + P_f(\quad)e^{\ i} \quad + P_f(2\quad)e^{\ i2} \quad + P_f(3\quad)e^{\ i3}\ \right) \tag{2.33}$$

$$= \frac{1}{4}\left(P_f(0) \quad iP_f(\quad) \quad P_f(2\quad) + iP_f(3\quad)\right).$$

It is interesting to note, that Scherer et al. performed signal isolation using mechanical choppers to isolate fluctuations in the total population arising from wave packet interference.[1,2] The delay-independent one-pulse contributions to the population were determined independently by blocking one of the incoming pulses and measuring the resulting population. Both one-pulse contributions to the population were then subtracted out of the fluctuating total population prepared using both pulse-pairs. Subsequent in-phase and in-quadrature measurements yielded the real and imaginary components of the bilinear interference. In contrast, the scheme presented by Eq. (2.31) or (2.32) removes any need for choppers in the signal isolation.

Molecular State Reconstruction

As shown in the preceding section, the linear WPI signal is equivalent to the time-dependent complex-valued overlap between a moving wave packet in an excited-electronic level and a stationary wave packet at the Franck-Condon point. As noted by Scherer et al.,[1] this information provides the time-dependent kernel necessary for calculating the resonance portion of the electronic absorption spectrum using the wave-packet formulation developed by Heller.[8] In their second paper, Scherer et al. additionally showed how measurements of the linear WPI signal can reveal the linear susceptibility.[2]

Several groups have also noted that linear WPI is a form of temporal coherent control, whereby the total population in an excited-electronic level is influenced via the bilinear wave packet interference.[9-15] Similar to other quantum control schemes, temporal coherent control relies on the interference between different quantum paths.[16] As we have shown above, a linear WPI experiment diagnoses the extent to which such interference effects exist. However, it is also possible to incorporate the incident pulses into the control mechanisms. [16-20] By shaping the incident pulses, in terms of either the temporal or spectral properties, each wave packet, and its dynamics, can be further manipulated.[17]

Leichtle et al. have considered a form of linear WPI in which one of the wave packets is prepared by a shaped pulse while preparation of the other wave packet occurs using a pulse of arbitrarily short duration. [3,4] The linear WPI signal then probes the time-dependent overlap of a shaped target wave packet with an unshaped reference wave packet. Moreover, in their development of quantum state holography (QSH), Leichtle et al. noted that the measured bilinear interference (see Eq. (2.31)) can be inverted to determine the shaped target wave packet, provided the energy eigenstates of the system are known. We now review the salient features of QSH.[21]

In QSH, the bilinear interference is measured over a range of the inter-pulse delay t_{21} with the mth measurement denoted as

$$z_m = \left\langle (2)_f \middle| (1)_f \right\rangle . \tag{2.34}$$

The measured interference is also equivalent to the overlap

$$z_m = \left\langle \text{ref}_2\left(\quad {}_g \right) \middle| \text{tar}_1\left(\quad {}_g \right) \right\rangle , \tag{2.35}$$

where the target state,

$$\left|\mathrm{tar}_1\left(\quad {}_g\right)\right\rangle = e^{i\ {}_1(\ {}_L)} P_1^{fg} \left|\ {}_g\right\rangle, \tag{2.36}$$

is prepared by the shaped first pulse and *not* propagated for the interpulse delay, and the reference wave packet,

$$\left|\mathrm{ref}_2\left(\quad {}_g\right)\right\rangle = e^{i\ {}_2(\ {}_L)\quad {}_L t_{21}} e^{iH_f t_{21}} P_2^{fg} e^{\ iH_g t_{21}} \left|\ {}_g\right\rangle, \tag{2.37}$$

is prepared by the presumedly unshaped second pulse and propagated *backwards* in time on the f surface. The target and reference states are not the one-pulse wave packets prepared by the first and second pulse, respectively. However, the overlap of Eq. (2.34) can be factored in any way which preserves its value. The factorization chosen by Leichtle et al. is advantageous as all the unknown information is placed into the target state, namely the effects which pulse shaping have on the preparation of a nuclear wave packet. In turn, all of the known information is placed into the reference state, including propagation under the presumedly known Hamiltonian H_f. The presence of the spectral phase factors in Eqs. (2.36) and (2.37) remove ambiguities in the definition of the target and reference wave packets, respectively, that are caused by shot-to-shot fluctuations in the absolute (or carrier-envelope offset) phase of each pulse, and therefore, each pulse propagator.

To implement reconstruction of the target state, the wave packets in Eqs. (2.36) and (2.37) are represented in a discrete position basis $\{|x_n\rangle\}$ composed of N elements equally spaced by a distance $\quad x$. With the completeness relation for this basis Eq. (2.35) is expressed as

$$z_m = \sum_{n=0}^{N} x \left\langle \mathrm{ref}_2\left(\quad {}_g \right) \middle| x_n \right\rangle \left\langle x_n \middle| \mathrm{tar}_1\left(\quad {}_g \right) \right\rangle . \tag{2.38}$$

The collection of M signal measurements is cast in matrix form as

$$\mathbf{z} = \mathbf{R}\mathbf{t} \ , \tag{2.39}$$

using the signal vector of Eq. (2.34), the reference matrix

$$R_{mn} = \left\langle \mathrm{ref}_2\left(\quad {}_g \right) \middle| x_n \right\rangle \quad x \tag{2.40}$$

and the unknown target vector

$$t_n = \left\langle x_n \middle| \mathrm{tar}_1\left(\quad {}_g \right) \right\rangle . \tag{2.41}$$

Each row of the reference matrix represents a different reference wave packet, and the corresponding signal point is the projection of the target state onto that reference wave packet.

To reconstruct the target vector from the interference signal, Eq. (2.39) is numerically inverted using the measured interference signal and the calculated reference matrix. Rows of the latter are calculated according to Eq. (2.40). However, the reference matrix may be singular. For the latter case, inversion of Eq. (2.39) is accomplished using singular value decomposition (SVD). The reference matrix is partitioned as

$$\mathbf{R} = \mathbf{U}\mathbf{W}\mathbf{V}^{\dagger} , \tag{2.42}$$

where the $N \quad N$ matrix $\mathbf{V}$ is unitary, the $M \quad N$ matrix $\mathbf{U}$ is row unitary, and the $N \quad N$ matrix $\mathbf{W}$ is diagonal with the jth singular value $W_{jj} \quad 0$. If any singular value is zero, the matrix $\mathbf{R}$ is singular and an inverse is not defined. However, a pseudo-inverse of $\mathbf{R}$ may be constructed as

$$\mathbf{R}_T^{\ 1} = \mathbf{V}\mathbf{W}_T^{\ 1}\mathbf{U}^{\dagger}, \tag{2.43}$$

in which a modified inverse of **W** is defined as

$$\left(\mathbf{W}_T^{\ 1}\right)_{jj} = \begin{matrix} 1/W_{jj} & \text{if} \quad W_{jj}/W_{\max} > T \\ 0 & \text{otherwise} \end{matrix} \tag{2.44}$$

where $W_{\max}$ is the maximum singular value and T is a chosen numerical tolerance. The solution to Eq. (2.39) is obtained by applying the pseudo-inverse of the reference matrix onto the signal vector yielding

$$\mathbf{r} = \mathbf{R}_T^{-1}\mathbf{z}\,. \tag{2.45}$$

The reconstructed vector obtained for a given value of T is the best solution to Eq. (2.39) in the least-squares sense: it minimizes the norm $|\mathbf{r}|$ and the residual $|\mathbf{z} \quad \mathbf{Rr}|$ of all possible solutions. As a measure of reconstruction accuracy, the fidelity of the reconstructed state is defined as

$$f = \left|\mathbf{r}^{\dagger} \quad \mathbf{t}\right| / \left(|\mathbf{r}| \quad |\mathbf{t}|\right), \tag{2.46}$$

and lies between 1 and 0. Experimentally, such a measure of accuracy is unobtainable, as it indicates prior knowledge of the target state. However, the fidelity is a useful measure of reconstruction accuracy when testing the proposed algorithm against known results.

In the next section, we simulate an application of the reconstruction procedure outlined above. We consider specific forms for the nuclear Hamiltonians of the g and f electronic levels and calculate the linear WPI interferogram. This provides an opportunity to test the accuracy and applicability of molecular state reconstruction using linear WPI data.

Model Harmonic System

In this section, we explore by example how features of the linear WPI signal reflect the relative motion of the excited wave packets and how QSH can be used to recover the stationary target state prepared by one of the pulses. We consider the example of a non-rotating, model diatomic molecule whose initial and final electronic levels are harmonic oscillators. The two electronic levels have different equilibrium configurations but the same angular frequency of vibration . This model system serves to demonstrate the main features of a linear WPI signal while providing analytical solutions for both the interference signal and the prepared vibrational wave packets. Figure 2.3 illustrates the relevant potential energy diagrams.

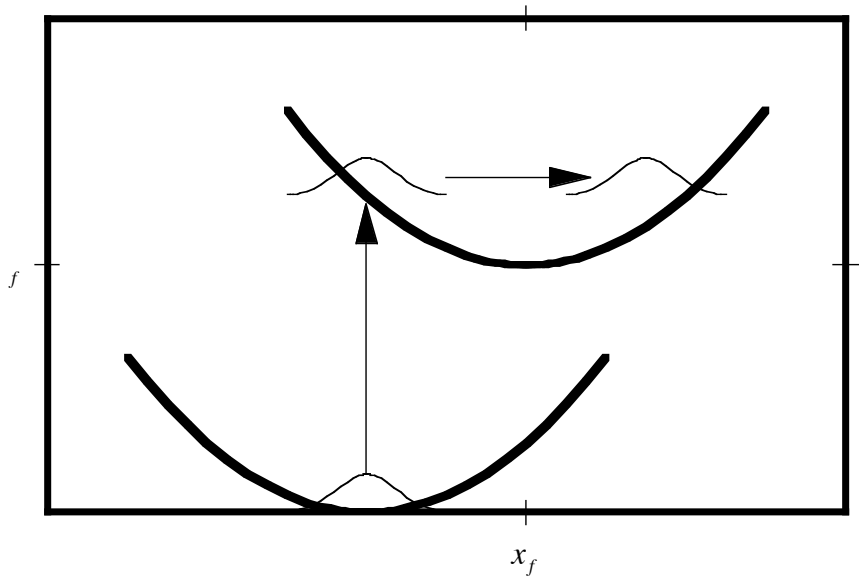

Fig. 2.3 The two harmonic potential surfaces used to describe the model molecule. The final surface has a larger bare electronic energy $_f$ and a larger equilibrium position x_f. The frequency of the oscillators is assumed to be the same. Preparation of a one-pulse wave packet is overlaid.

For the initial electronic level, the Hamiltonian is

$$H_g = \frac{p^2}{2} + \frac{\quad^2}{2} x^2 \tag{2.47}$$

with p the momentum, the mass of the oscillator, and x the relative displacement about the equilibrium position. The ladder operator

$$a = \frac{\quad}{2}^{1/2} \quad x + i\frac{p}{\quad} \quad , \tag{2.48}$$

which obeys the commutation relation

$$a, a^{\dagger} \quad = 1 , \tag{2.49}$$

is used to express the g-state Hamiltonian as[5]

$$H_g = \quad a^{\dagger} a + \frac{1}{2} \quad . \tag{2.50}$$

The energy eigenstates of g satisfy

$$H_g |n\rangle = E_g(n) |n\rangle , \tag{2.51}$$

where $n = 0,1,2,...$ is the quantum of vibrational excitation and

$$E_g(n) = \quad (n + 1/2) \tag{2.52}$$

is the eigenenergy of the nth eigenstate.

The f-state Hamiltonian is similarly taken as

$$H_f = \frac{p^2}{2} + \frac{\quad^2}{2}(x \quad x_f)^2 + \quad_f , \tag{2.53}$$

where x_f is the relative displacement in equilibrium position and $\quad_f$ is the bare electronic energy difference between *f* and *g*. In Appendix A, we show the *f*-state Hamiltonian can be expressed as

$$H_f = D\left(\quad_f \right)\left(H_g + \quad_f \right) D^{\dagger}\left(\quad_f \right), \tag{2.54}$$

where $\quad_f = \left(\quad / 2 \right)^{1/2} x_f$ and

$$D\left(\quad \right) = e^{\quad a^{\dagger} \quad a} \tag{2.55}$$

is the unitary displacement operator defined in terms of the dimensionless (complex) number . It is straightforward to show that the energy eigenstates of *f* are then

$$\left| \bar{n} \right\rangle = D\left(\quad_f \right) \left| n \right\rangle \tag{2.56}$$

and have eigenenergies

$$E_f\left(n\right) = E_g\left(n\right) + \quad_f . \tag{2.57}$$

To analyze generic features of the linear WPI signal, we specialize to the case that the pulse durations are significantly shorter than any time scale for nuclear dynamics in either electronic level. As we will show, this impulsive approximation to electronic excitation neglects shaping of the prepared wave packets which might occur either deliberately through the properties of the pulses or consequentially through nuclear dynamics during the field-matter interaction.

To investigate the impulsive limit, we express the transition amplitude for the pulse propagator (2.18) in the position eigenbasis as

$$\left\langle x \left| P_j^{fg} \right| x \right\rangle = i \quad d \left\langle x \left| e^{iH_f} \quad_{fg} \mathbf{e}_j e^{\quad iH_g} \right| x \right\rangle A_j\left(\quad \right) \cos \quad_j \left(\quad \right).$$

Owing to the (assumed) ultrashort nature of the temporal envelope, nuclear dynamics that transpire during the pulse interactions are negligible and the latter equation can be reduced to

$$\langle x\,|P_j^{fg}|x\rangle = i\langle x\,|\;{}_{fg}\;\mathbf{e}_j|x\rangle\left(d\;e^{i\;{}_f}\;A_j(\;)\cos\;{}_j(\;)\right. \tag{2.58}$$

$$= i\;{}_{fg}(x)\;\mathbf{e}_j\;{}_j\left(\;{}_f\right)e^{\;i\;{}_j(\;{}_f)}\;(x\quad x),$$

where (x) is the Dirac delta function. By neglecting the coordinate dependence of the transition dipole-moment function the pulse propagator reduces in the impulsive approximation to the constant

$$P_j^{fg} = i\;{}_{fg}\;{}_j e^{\;i\;{}_j}, \tag{2.59}$$

where ${}_j = {}_j\left(\;{}_f\right)$, ${}_j = {}_j\left(\;{}_f\right)$ and ${}_{fg} = {}_{fg}\;\mathbf{e}_j$. Note that that the validity of the impulsive approximation results from general considerations about the brevity of the pulses with respect to the nuclear dynamics and is independent of the harmonic model.

From Eq. (2.59), the one-pulse wave packets are then approximated as

$$\left|(1)_f\right\rangle = i\;{}_{fg}\;{}_1 e^{\;i\;{}_1} e^{\;iH_f t_{21}}\left|n\right\rangle \tag{2.60}$$

and

$$\left|(2)_f\right\rangle = i\;{}_{fg}\;{}_2 e^{\;i\;{}_2} e^{\;iH_g t_{21}}\left|n\right\rangle. \tag{2.61}$$

The form of Eqs. (2.60) and (2.61) show the one-pulse wave packets are scaled copies of the originally vibrational state propagated for t_{21} on the *f* and *g* potential energy surfaces, respectively. This simplification arises from neglecting the finite duration of the pulses.

To further investigate the form of the wave packets we recall the identity for the *f*-state Hamiltonian given by Eq. (2.54). With the results from Appendix A, Eq. (2.60) becomes

$$\left|(1)_f\right\rangle = i \quad {}_{fg} \quad {}_1 e^{\quad i \quad {}_1 \quad iE_f(n)t_{21} \quad i \quad {}_f^2 \sin \quad t_{21}} D\left(\quad {}_f\left(1 \quad e^{\quad i \quad t_{21}}\right)\right)\left|n\right\rangle \tag{2.62}$$

and the wave functions of the one-pulse wave packets are

$$\left\langle x\middle|(1)_f\right\rangle = i \quad {}_{fg} \quad {}_1 e^{\quad i \quad {}_1 \quad iE_f(n)t_{21} \quad i \quad {}_f^2 \sin \quad t_{21}} e^{\quad ip_1\left(x_1/2 \quad x\right)} \left\langle x \quad x_1\middle|n\right\rangle \tag{2.63}$$

and

$$\left\langle x\middle|(2)_f\right\rangle = i \quad {}_{fg} \quad {}_2 e^{\quad i \quad {}_2 \quad iE_g(n)t_{21}} \left\langle x\middle|n\right\rangle . \tag{2.64}$$

Here $\left\langle x\middle|n\right\rangle$ is the wave function of the nth harmonic oscillator eigenstate centered about the *g*-state equilibrium position. In contrast, the one-pulse wave packet $\left|(1)_f\right\rangle$, which has propagated in the displaced potential for t_{21}, is centered at

$$x_1 = x_f\left(1 \quad \cos \quad t_{21}\right) \tag{2.65}$$

and has the corresponding average momentum

$$p_1 = m \quad x_f \sin \quad t_{21} . \tag{2.66}$$

The latter results are equivalent to the trajectory of the corresponding classical system.[5]

We calculate the interference signal by overlapping the one-pulse wave packets obtained in Eqs. (2.60) and (2.61) to yield

$$\left\langle (2)_f\middle|(1)_f\right\rangle = \quad {}_{fg}^2 \quad {}_1 \quad {}_2 e^{i\left(\quad {}_2 \quad {}_1 \quad {}_f t_{21}\right)} \left\langle n\middle|e^{iH_g t_{21}} e^{\quad iH_f t_{21}}\middle|n\right\rangle . \tag{2.67}$$

The form of Eq. (2.67) emphasizes the role played by the wave-packet dynamics in a linear WPI experiment and the use of the bilinear interference as the auto-correlation

function essential to using the wave-packet formalism for calculating the electronic absorption spectrum.[8] Inserting (2.60) into (2.67), the wave-packet interference becomes

$$\left\langle (2)_f \middle| (1)_f \right\rangle = {}^{2}_{fg} \quad {}_{1} \quad {}_{2} e^{i\left({}_{2} \quad {}_{1} \quad {}_{f} t_{21} \right)} \tag{2.68}$$

$$\langle n | D\left(\quad {}_{f} \left(1 \quad e^{\ i \ t_{21}} \right) \right) | n \rangle e^{\ i \ {}^{2}_{f} \sin(\ t_{21})},$$

which, using the following result from Appendix A

$$\langle n | D(\quad) | n \rangle = e^{\ | \ |^2 / 2} L_n \left(| \quad |^2 \right),$$

where $L_n(x)$ is the Laguerre polynomial, reduces to

$$\left\langle (2)_f \middle| (1)_f \right\rangle = {}^{2}_{fg} \quad {}_{1} \quad {}_{2} e^{i\left({}_{L} \quad {}_{f} \right) t_{21}} \tag{2.69}$$

$$\exp \quad {}^{2}_{f} \left(e^{\ i \ t_{21}} \quad 1 \right) (L_n \left(2 \quad {}^{2}_{f} \left(1 \quad \cos \quad t_{21} \right) \right).$$

In going to Eq. (2.69) we have used the phase-locking condition given in Eq. (2.7) and the fact that the interference is defined for the case $= 0$; therefore ${}_{2} \quad {}_{1} = {}_{L} t_{21}$. Notice the locking frequency demodulates the wave packet interference away from the otherwise rapidly oscillating electronic frequency ${}_{f}$; the linear WPI signal varies on the much slower time scale of vibrational motion, $= 2 \quad / \quad$. In Fig. 2.4, we plot the linear interference signal given by Eq. (2.69), taking $n = 0$, ${}_{L} = {}_{f}$ and ${}^{2}_{f} = 2$.

In Fig. 2.4, the real component of the interference signal peaks at integral multiples of , while the imaginary component vanishes for half-integral multiples of . These features can be understood in terms of the one-pulse wave packets moving in a out of coincidence with each other. For integral values of the delay both wave packets are localized at the inner turning point, while for odd-half-integral multiples of the delay the

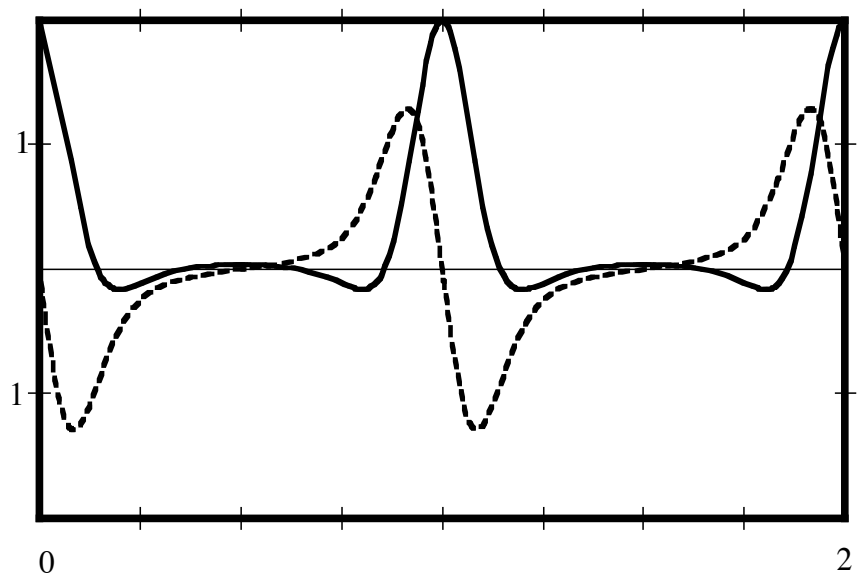

Fig. 2.4 The linear WPI signal for a harmonic oscillator system. Time is plotted in units of vibrational period . Solid lines denote the real component, dashed lines denote the imaginary component. The signal is plotted in units of $^{2}_{fg\ 1\ 2}$.

wave packets are at opposite turning points. In each case, the classical momentum (2.66) vanishes and, from the phase of Eq. (2.69), we expect the imaginary component of the interference signal to vanish as well. In contrast, the real component of the interference signal peaks when the amplitude of the wave packets are coincidence, with a maximal value occurring when both wave packets are at the inner turning point.

Coincidence of the wave packets can be visualized using phase-space diagrams. We define the Wigner phase-space distribution function of a state $|\ \ \rangle$ as

$$W(x,p) = \frac{1}{2}\quad dq\langle x\quad q/2|\ \ \rangle\langle\ \ |x+q/2\rangle e^{ipq}\,. \tag{2.70}$$

After normalization, the first-pulse wave packet in Eq. (2.63) is represented in phase space as

$$W_1(x,p) = \frac{1}{\ }\exp\left\{ \frac{1}{4m} \left(p \quad p_1\right)^2 + m^2 \quad {}^2\left(x \quad x_1\right)^2 \right. \begin{matrix} + \\ - \end{matrix} \tag{2.71}$$

while the second-pulse wave packet in Eq. (2.64) is

$$W_2(x,p) = \frac{1}{\ }\exp\left\{ \frac{1}{4m} \quad p^2 + m^2 \quad {}^2x^2 \right. \begin{matrix} + \\ - \end{matrix}. \tag{2.72}$$

In Fig. 2.5, the one-pulse wave packets are plotted in phase-space for different amounts of interpulse delay. Panels (a) through (d) represent the first-pulse wave packet (gray lines) moving clockwise about the *f*-state minimum, while the second-pulse wave packet (black lines) is localized at the Franck-Condon point. The target and reference states in used in QSH are exactly opposite, with the moving reference wave packet propagating backward in time. From Eqs. (2.36) and (2.37) we find the position representation of the target and reference wave packets are

$$\left\langle x_p \middle| \mathrm{tar}_1 \right\rangle = i \quad {}_{fg} \quad {}_1\left\langle x_p \middle| n \right\rangle \tag{2.73}$$

and

$$\left\langle x_k \middle| \mathrm{ref}_{2,m} \right\rangle = i \quad {}_{fg} \quad {}_2 e^{i\left(\quad {}_L \quad {}_f \right)t_{21} + i \quad {}_f^2 \sin \quad t_{21}} \left\langle x \quad x_1 \middle| n \right\rangle e^{ip_1\left(x_1/2 \quad x\right)}, \tag{2.74}$$

respectively. The target state for the case of an arbitrarily short pulse is a scaled copy of the initial vibrational wave packet, localized at the Franck-Condon transition point. The reference state propagates counter-clockwise in phase space for increasing inter-pulse delay, and sample the shape of target state distribution. Like the gray one-pulse wave packet in Fig. 2.5, the reference wave packets lie along a single energy shell which, for this simplified case, directly intersects the target state at the Franck-Condon point. More interesting scenarios are also possible when shaped pulses are used.[3,4]

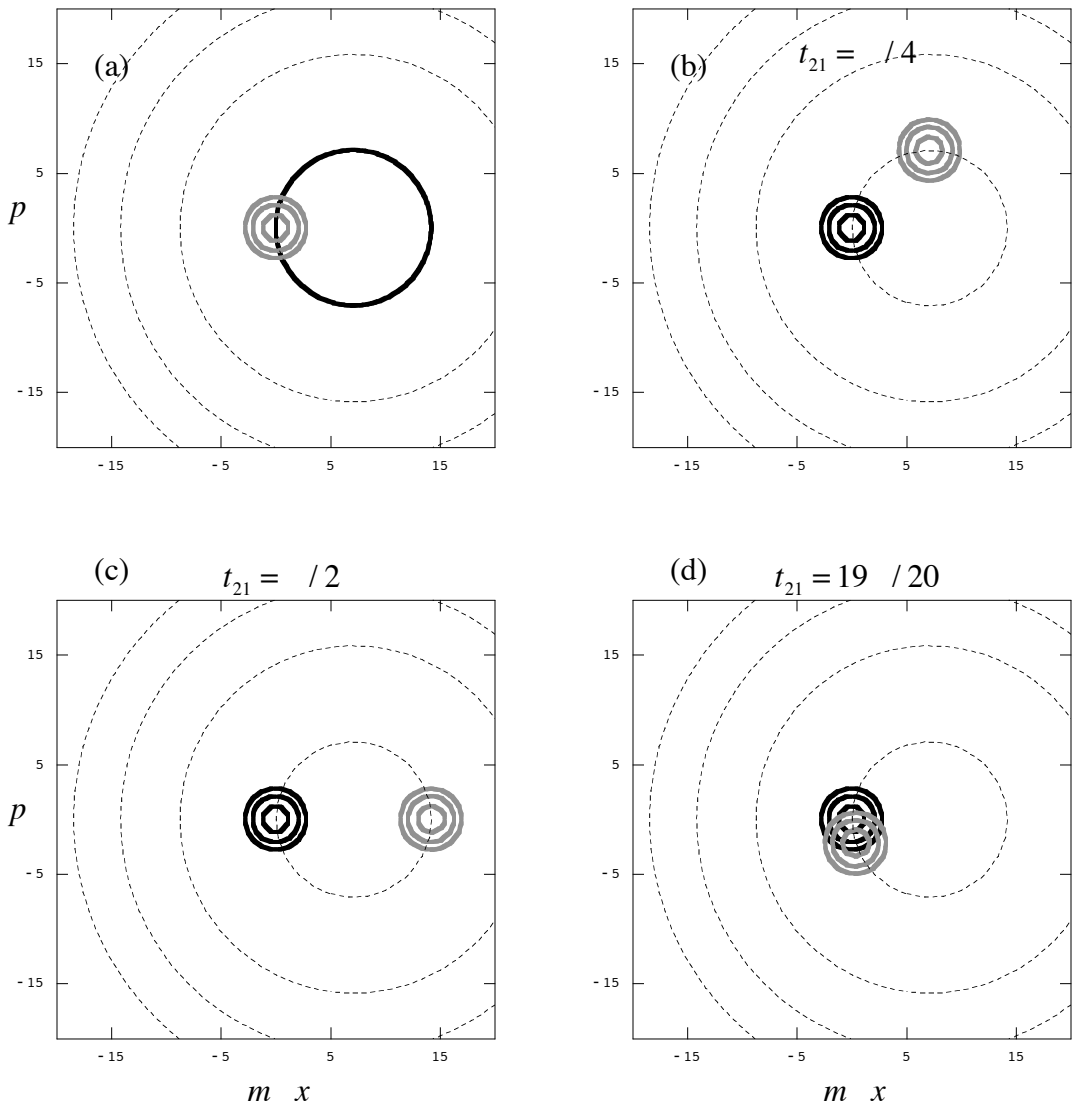

Fig. 2.5 Phase-space diagrams of the one-pulse wave packets for various t_{21} with isoenergy contours (dashed lines) of the harmonic *f*-state potential underlain; $^{2}_{f} = 2$, $m = 1$ and $= 2$. (a) The first-pulse wave packet (gray lines) traces clockwise the circle shown. (b) Phase space separations are often larger than configurational changes. (c) Maximal displacement occurs when the wave packets at opposite turning points. (d) A recurrence in phase-space coincidence results in a peak in the interference signal.

To demonstrate target state reconstruction, we calculate the reference wave packets in Eq. (2.74) to construct the reference matrix of Eq. (2.40). We use a position grid spanning from $3x_f$ to $3x_f$ in steps of 0.1 Å over the range of interpulse delays from 0 to 2 in steps 0.01 . Each calculated reference wave packet is stored in a row of the reference matrix. Calculating the pseudo-inverse with a tolerance of 0.1 and applying it to the simulated interferogram yields a reconstructed state with a fidelity of 0.9986, a near perfect reconstruction of the actual target wave packet. With the addition of 5% random Gaussian noise to the signal, a fidelity of 0.9969 is obtained. The latter result, shown in Fig. 2.6, has a decreased fidelity since noise washes out fine features in the interferogram and leads to a significant distortion of the reconstructed phase function.

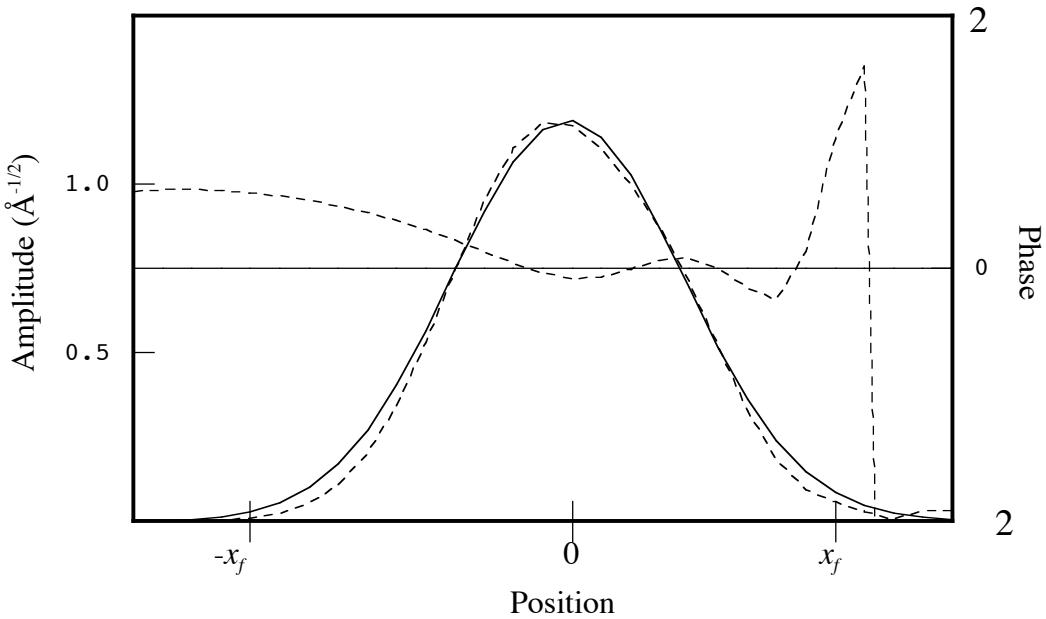

Fig. 2.6 Target and reconstructed wave packets for the model harmonic system. Solid lines represent the amplitude and phase of the target state as a function of position, while dashed lines represent the same for the reconstructed state. The target-state amplitude is localized about 0 Å, the Franck-Condon point on the *f* surface, while the target-state phase is flat, representing zero momentum. The reconstructed amplitude is also localized about 0 Å, and has a phase which is approximately constant across the region of non-negligible target-state amplitude.

Remarks

Leichtle et al. have simulated applications of QSH for reconstructing shaped vibrational wave packets in a non-rotating sodium dimer and found that very accurate reconstructions of certain target states are possible, i.e. high fidelities.[3,4] There are, however, limitations as to what target wave packets can be accurately reconstructed using QSH. First, the potential energy surface on which the wave packet is prepared must be characterized in sufficient detail to permit accurate calculations of the reference wave packets which propagate of that surface. Second, reconstruction accuracy is limited to spatial regions where both the target and reference states have nonzero amplitude. Since the reference wave packets are confined to propagate along a single (Franck-Condon) energy shell, as illustrated in Fig. 2.5, opportunities for reconstruction are limited to the region immediately about the Franck-Condon point. As noted by Leichtle et al., the same issue arises from considerations of the pulse bandwidths; if the first pulse, which prepares the target state, has a larger bandwidth than the second pulse, the targeted superposition state prepared by the first pulse will include population in nuclear eigenstates which can not be excited by the second pulse.

Even with these limitations, QSH is an attractive experimental means for identifying shaped wave packets and can be used to provide feedback to adaptive pulse-shaping control techniques. Experimentally, Bucksbaum and coworkers have used a variation of QSH for shaping electronic Rydberg wave packets in cesium atoms.[23] In those experiments, the electronic wave packet prepared by an ultrashort pulse was probed by measuring the population of each contributing electronic level. From the known

eigenenergies of the electronic states and the interpulse delay time, the target wave packet was reconstructed. The measured wave function was then used as input into a closed-loop feedback-controlled pulse shaper, programmed to shape the electronic wave packet to a specific form. Applied to a molecular system, such a technique could support tailored investigations of the difference in molecular dynamics arising from differently shaped initial states.

Yet, the requirement that the excited-electronic-level nuclear Hamiltonian be well characterized obviates any practical need for experimental state reconstruction. Given the actual molecular Hamiltonian, computational approaches to quantum control can be used to complement experimental pulse-shaping techniques.[18-20] Though the size of the molecular system limits the molecules for which computational approaches are applicable, the need to calculate reference wave packets imposes the same restriction on the approach taken by QSH.

Notes

1. N. F. Scherer, R. J. Carlson, A. Matro, M. Du, A. J. Ruggiero, V. Romero-Rochín, J. A. Cina, G. R. Fleming, and S. A. Rice, J. Chem. Phys. **95**, 1487 (1991).

2. N. F. Scherer, A. Matro, L. D. Ziegler, M. Du, R. J. Carlson, J. A. Cina, and G. R. Fleming, J. Chem. Phys. **96**, 4180 (1992).

3. C. Leichtle, W. P. Schleich, I. Sh. Averbukh, and M. Shapiro, Phys. Rev. Lett. **80**, 1418 (1998).

4. I. Sh. Averbukh, M. Shapiro, C. Leichtle, and W. P. Schleich, Phys. Rev. A **59**, 2163 (1999).

5. C. Cohen-Tanoudji, B. Diu, and F. Lahoë, *Quantum Mechanics* (John Wiley and Sons, New York, 1977).

6. G. P. Tolstov, *Fourier Series*, (Dover Publications, New York, 1962).

7. W. H. Press, S. A. Teukolsky, W. T. Vetterling, and B. P. Flannery, *Numerical Recipes in C* (Cambridge University Press, Cambridge, 1988).

8. E. J. Heller, in *Advances in Classical Trajectory Methods*, edited by W. L. Hase (JAI Press, London, 1992).

9. V. Blanchet, C. Nicole, M. A. Bouchene, and B. Girard, Phys. Rev. Lett. **78**, 2716 (1997).

10. M. A. Bouchene, V. Blanchet, C. Nicole, N. Melikechi, B. Girard, H. Ruppe, S. Rutz, E. Schreiber, and L. Wöste, Eur. Phys. J. D **2**, 131 (1998).

11. M. A. Bouchène, C. Nicole, and B. Girard, J. Phys. B **32**, 5167 (1999).

12. V. Blanchet, M. A. Bouchène, and B. Girard, J. Chem. Phys. **108**, 4862 (1998).

13. K. Ohmori, Y. Sato, E. E. Nikitin, and S. A. Rice, Phys. Rev. Lett. **91**, 243003 (2003).

14. M. Gühr, H. Ibrahim, and N. Schwenter, Phys. Chem. Chem. Phys. **6**, 5353 (2004).

15. F. Milota, J. Sperling, V. Szöcs, A. Tortschanoff, and H. F. Kauffmann, J. Chem. Phys. **120**, 9870 (2004).

16. R. J. Gordon and S. A. Rice, Annu. Rev. Phys. Chem. **48**, 601 (1997).

17. M. Shapiro and P. Brumer, *Principles of Quantum Control of Molecular Processes* (Wiley-Interscience, Hoboken, N. J., 2003).

18. R. S. Judson and H. Rabitz, Phys. Rev. Lett. **68**, 1500 (1992).

19. H. Rabitz, R. de Vivie-Riedle, M. Motzkus, and K. Kompa, Science **288**, 824 (2000).

20. C. Daniel, J. Full, L. González, C. Lupulescu, J. Manz, A. Merli, Š. Vajada, and L. Wöste, Science **299**, 536 (2003).

21. In order to facilitate comparison between QSH and our conceptually similar reconstruction technique discussed in subsequent chapters, our review of QSH here does not use the notation found in Refs. [16] and [17]. For instance, we use the discrete position basis to construct representations of the target and reference states, while in the original work, Leichtle et al. performed their analysis using the energy eigenstates. However, the salient concepts are independent of representation.

22. I. S. Gradshteyn and I. M Rayzhik, *Table of Integrals, Series, and Products* (Academic Press, New York, 1995) 5th Ed.

23. T. C. Weinacht, J. Ahn, and P. H. Bucksbaum, Nature **397**, 233 (1999).